Supplementary Information:

Microdomains and stress distributions in bacterial monolayers on curved interfaces

Blake Langeslay[1] and Gabriel Juarez[2]

Image processing methods – construction of director field and detection of defects.

Experimental images were first processed with ImageJ to subtract background artifacts with the built in rolling ball background subtraction. The background-subtracted image I_0 was processed with a Wiener filter and then a Gaussian filter to eliminate visual noise. The gradient brightness of the resulting image $I_{filtered}$ was then calculated to identify orientations of cell edges, with the gradient pointing perpendicular to the cell edge.

This gradient's orientation angle was rotated by π to point parallel to the cell edge, and multiplied by 2 to account for the nematic symmetry of the cells, before being decomposed into x and y components. The vector components were then smoothed using a Gaussian filter. Finally, the components were converted back into an angle, which was divided by two to convert back into the real director orientation, and the resulting director field was downsampled to approximately match the cell density.

This director field was analyzed using the method described in Decamp et al. to identify topological defects. In brief, the area around a test point was segmented into sections, and the average orientation in each section was computed. Progressing clockwise through the sections, we checked for a net difference of plus or minus pi. This resulted in clusters of "detected" points around each actual defect, which were then grouped via the "clusterdata" algorithm in MATLAB. The centroids of these clusters were taken as the actual locations of the defects.

Supplementary Video descriptions

SV1: Timelapse of *A. borkumensis* growth on a flat oil-water interface. Images were taken at 2 minute intervals via phase contrast microscopy at 60x magnification. Scale bar is 100 μm; 1 second of video = 40 minutes of experimental time.

SV2: Simulation of bacterial growth on a flat interface. Cell aspect ratio is 4.9. Cell colors correspond to orientation angle (as shown in colorwheel). Scale bar is 20 μm.

SV3: Simulation of bacterial growth on a spherical surface. Cell aspect ratio is 4.9; surface curvature is 0.0025 μm^{-2}. Cell colors correspond to angle with respect to the vector pointing "north" at the cell's location, with the north pole set at (0,0) – so light blue cells point along lines of longitude while red cells point along lines of latitude.

SV4: Simulation of bacterial growth on a spherical surface. Cell aspect ratio is 4.9; surface curvature is 0.01 μm^{-2}. Cell color represents the parallel stress normalized by the mean stress for each simulation frame, as indicated by the colorbar.

SV5: Simulation of bacterial growth on a spherical surface. Cell aspect ratio is 6.7; surface curvature is 0.01 μm^{-2}. Cell color represents the parallel stress normalized by the mean stress for each simulation frame, as indicated by the colorbar.

SV6: Simulation of bacterial growth on a spherical surface. Cell aspect ratio is 4.9; surface curvature is 0.0025 μm^{-2}. Cell color represents the parallel stress normalized by the mean stress for each simulation frame, as indicated by the colorbar.

SV7: Simulation of bacterial growth on a spherical surface. Cell aspect ratio is 6.7; surface curvature is 0.0025 μm^{-2}. Cell color represents the parallel stress normalized by the mean stress for each simulation frame, as indicated by the colorbar.

Supplementary Figures

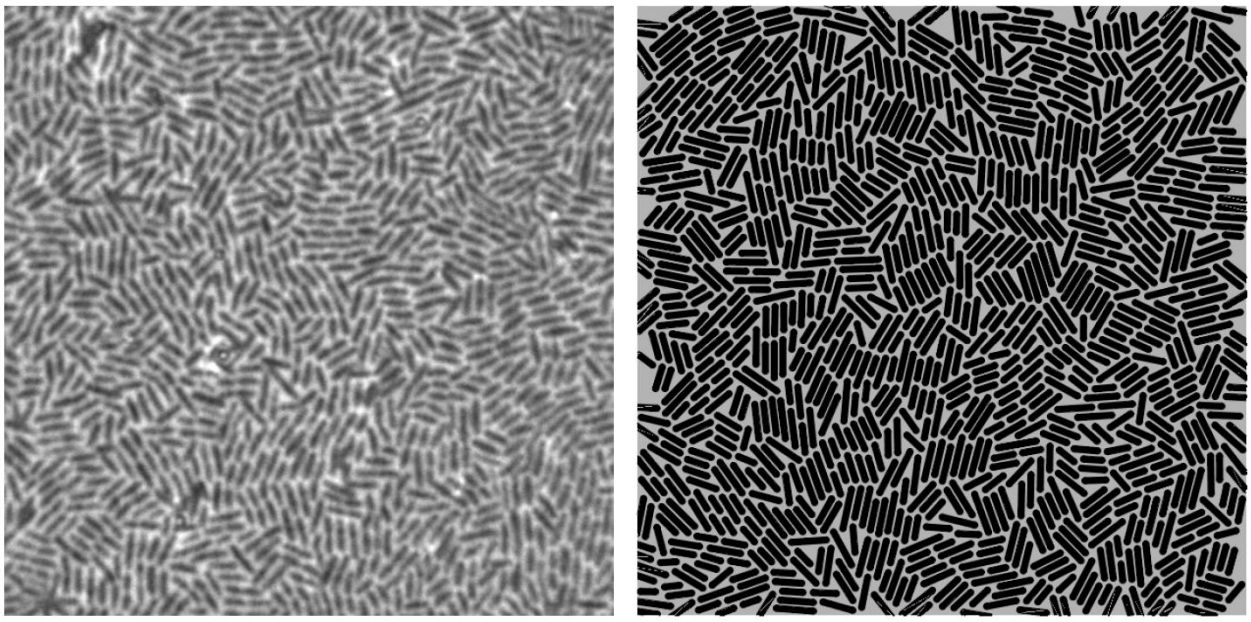

Fig. S1: Comparison of colony structure between experiments (left) and simulations (right). Both images are taken at the point of homogeneous coverage.

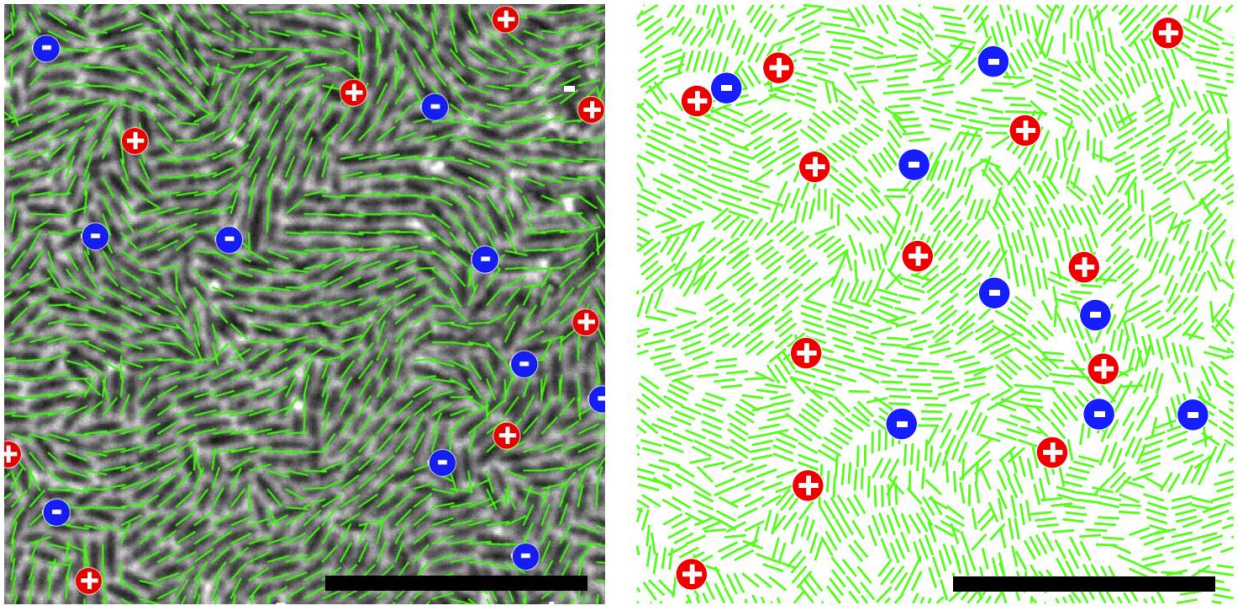

Fig. S2: Sample director fields and defect locations in cell monolayers in flat (zero curvature) interfaces for (left) experiments and (right) simulations. Scale bars are 20 μm.

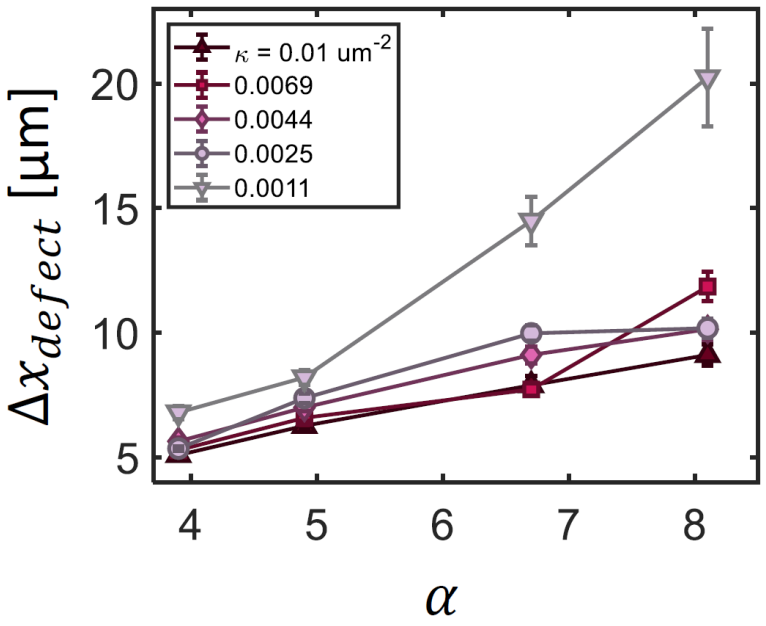

Fig. S3: Plots of the mean defect separation for different cell aspect ratios α and surface curvatures. Defect separation increases with increasing cell aspect ratio for all curvatures. Error bars are standard error.

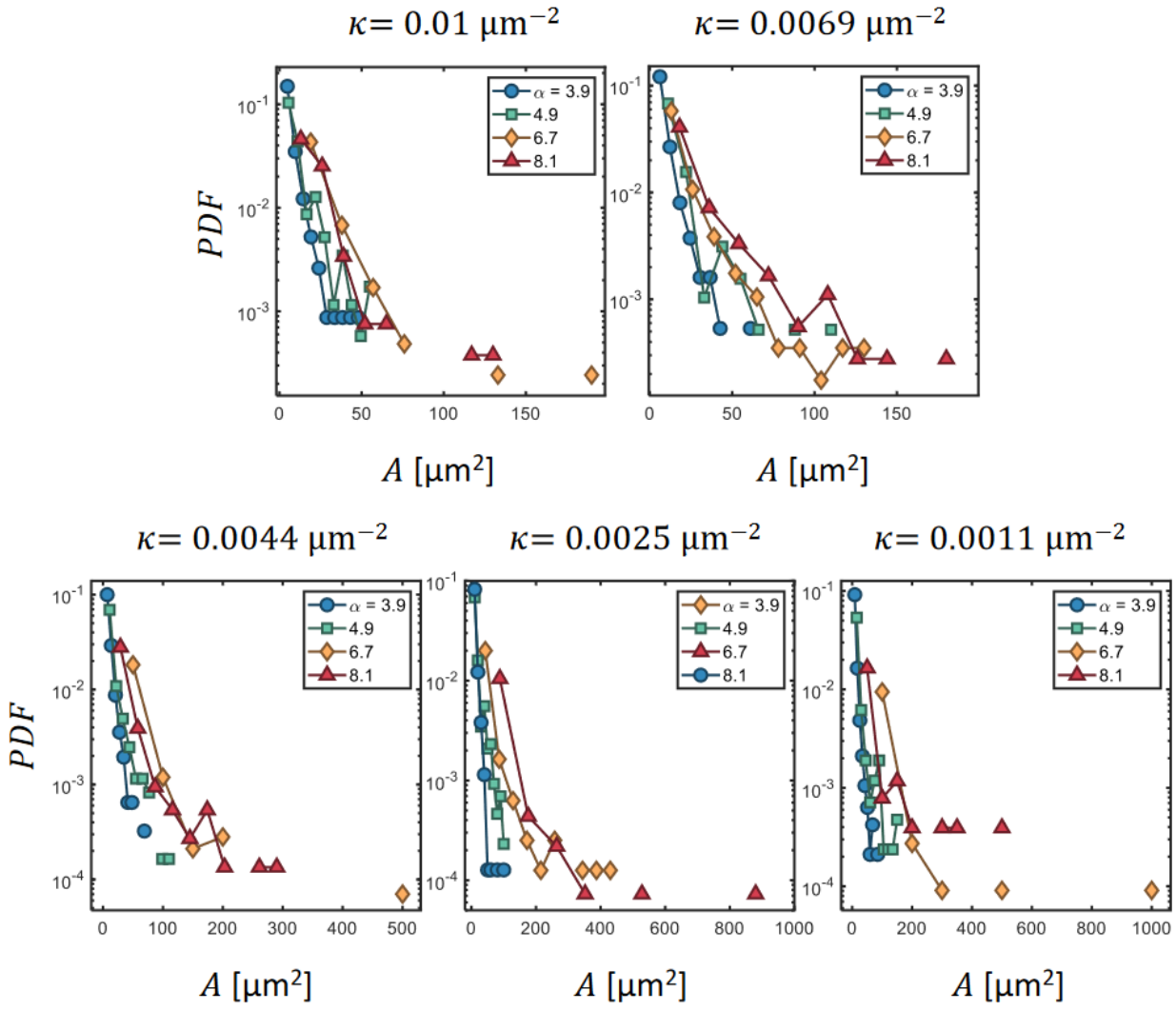

Fig. S4: Probability distributions of microdomain areas for all combinations of surface curvature κ and aspect ratio α.

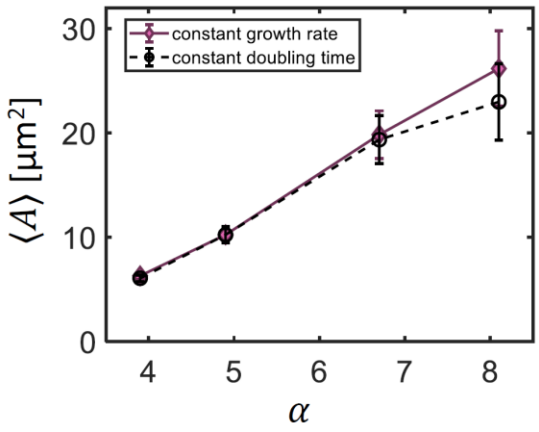

Fig. S5: Comparison of the relationship between microdomain area and aspect ratio at curvature $\kappa = 0.0044\ \mu m^{-2}$, for constant growth rate 2 μm/hr (data used in the body of the paper) and constant doubling time 2 hrs. Constant doubling time results in comparatively lower areas at higher aspect ratio, but the trend is the same in either case. Error bars are standard error.

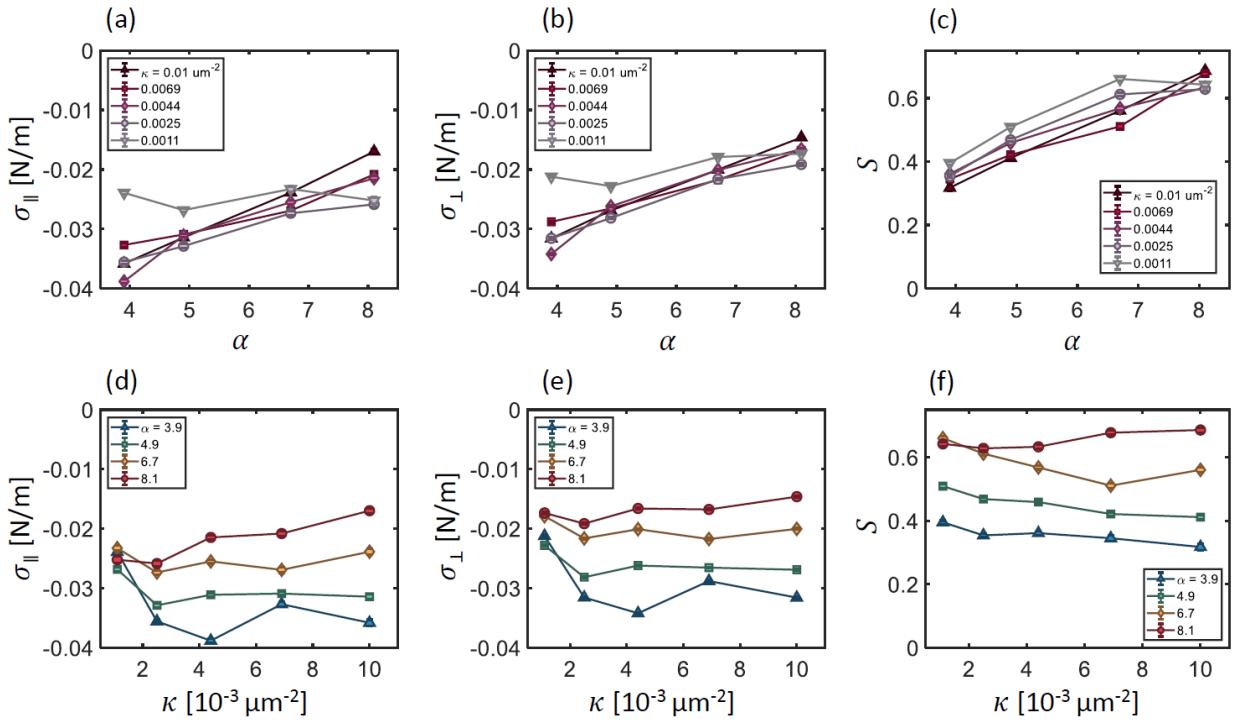

Fig. S6: Plots of the parallel stresses, perpendicular stresses, and average order *S* at varying cell aspect ratios (a-c) and substrate curvatures (d-f). Plots (a) and (b) show that the magnitude of both stress components decreases with increasing aspect ratio at all curvatures, and that the perpendicular stress consistently has lower magnitude than the parallel stress. Plot (c) shows that order increases with increasing aspect ratio. Plots (d-f) show no clear dependence of stress or order on curvature. All error bars represent standard error.

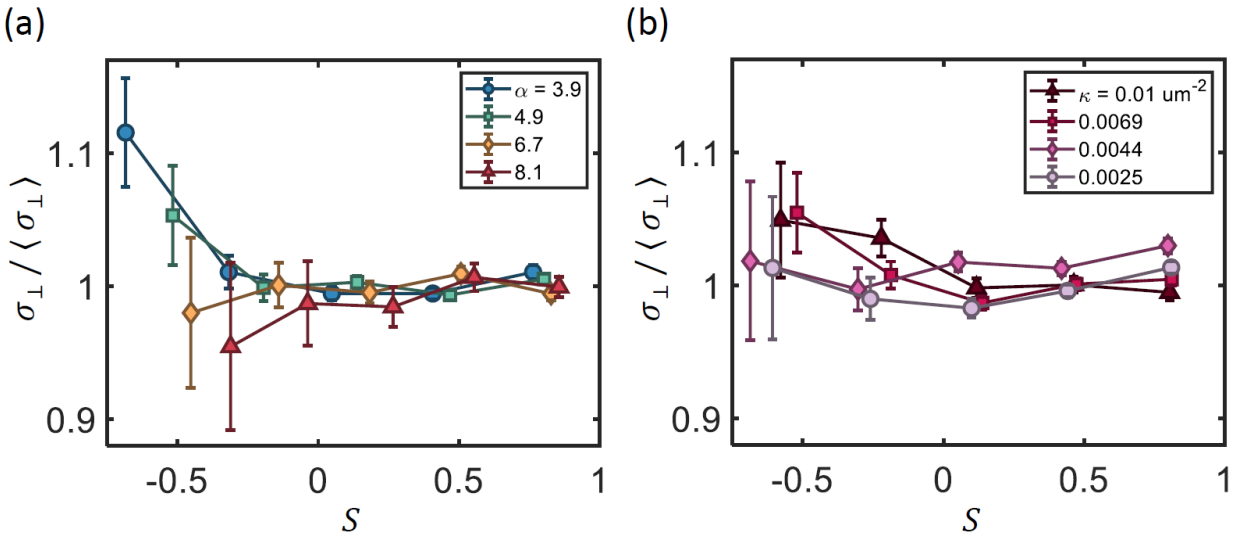

Fig. S7: Perpendicular component of stress, binned by order *S* and normalized by the mean perpendicular stress, aggregated over each aspect ratio (a) and curvature (b). Unlike the parallel stress, the perpendicular stress exhibits no consistent behavior with respect to order. All errobars represent standard error.

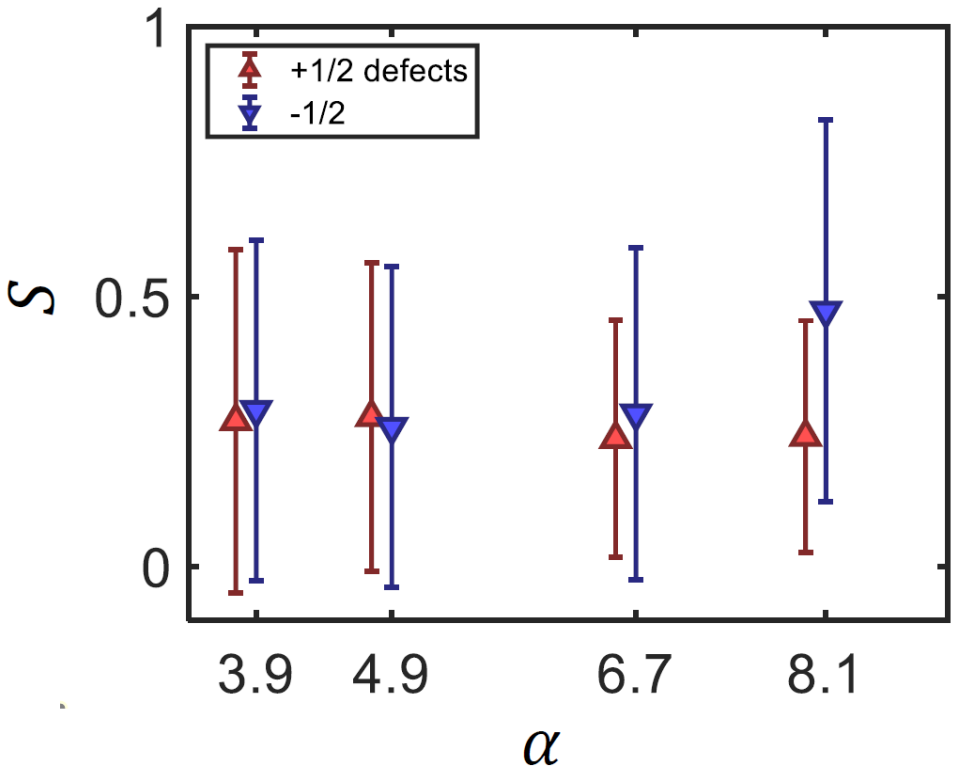

Fig. S8: Average order near topological defects at different aspect ratios. Error bars are standard deviation. All near-defect orders are lower than the average order for their respective aspect ratio.

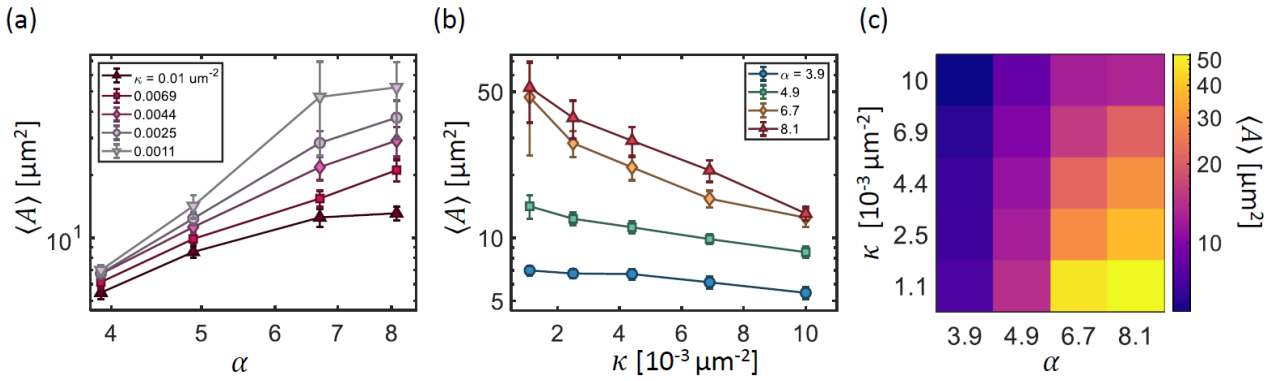

Fig. S9: Microdomain data at packing fraction $\phi = 1.1$. Mean microdomain areas plotted against aspect ratio (a) and curvature (b), and a heatmap (c) showing all areas across the simulated parameter space. Results are very similar to those for $\phi = 1.05$. Error bars are standard error.

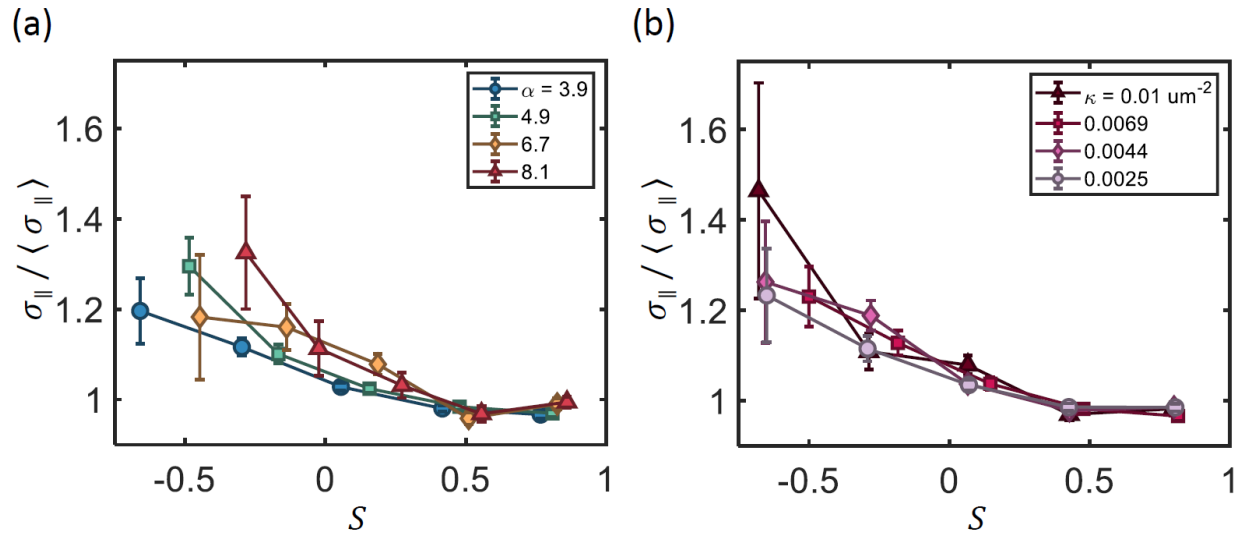

Fig. S10: Parallel component of stress, binned by order *S* and normalized by the mean parallel stress, aggregated over each aspect ratio (a) and curvature (b), at $\phi = 1.1$. The parallel exhibits similar behavior to that demonstrated at $\phi = 1.05$, with consistently higher stress at low order across all aspect ratios and curvatures. All errobars represent standard error.